Soft X-Ray Tomography for the Study of MHD Instability Mode and Impurity Transport*)

Dong LI, YunBo DONG, Wei DENG, WuLv ZHONG and Min XU

Southwestern Institute of Physics, Chengdu, Sichuan, 610041, People's Republic of China

(Received 25 December 2021 / Accepted 22 February 2022)

An advanced tomography method based on Bayesian probability theory is presented in this article. In the method, Gaussian Process (GP) prior is adopted as an effective approach to smoothness regularization which can be optimized based on the balance between model complexity and data constraint. In particular, to address the problem of varying smoothness in space, a non-stationary version of the GP has been developed and resolved via Bayesian hierarchical algorithm to implement locally adaptive smoothness regularization such that the accuracy of the reconstruction can be improve significantly. The Bayesian formulism allows the reliability of the reconstruction result to be examined by the confidence interval of a posterior probability. Through a wide range of applications, this tomography method is proved to be a robust tool for the study of magnetohydrodynamics (MHD) activity and impurity transport during HL-2A experimental campaigns.

Keywords: tomography, Bayesian probability theory, Gaussian Process, magnetohydrodynamics

DOI: 10.1585/pfr.17.2402028

1. Introduction

In nuclear fusion research, a variety of diagnostic systems have been devised to measure the continuum radiation in specific energy ranges, typically including the soft/hard X-ray emission as well as the line radiation emitted by impurity particles. In practice, the detector arrays of a diagnostic system have to be located outside the plasma and collect photons/particles along the viewing chords. As a consequence, only line-integrated measurements can be carried out. In order to extract local information of the measured radiation, tomography algorithms have to be developed for such diagnostics for the reconstruction of a 2D emission distribution from a limited number of line-integrated data. The difficulty of solving the tomography problem, which is essentially an ill-posed inversion problem, mainly arises from the sparse coverage of viewing chords and the error subjected to the measured data.

To date, a large number of tomography methods have been developed and applied especially for fusion diagnostics with both advantages and disadvantages on specific circumstance. In the early stage, Abel inversion [1] is one of the most used method with an assumption of circular symmetry which imposes a beneficial constraint on the reconstruction when the diagnostic system has multiple lines-of-sight (LOS) from a single direction, which however would be invalid for the configuration with a non-circular plasma cross-section. Since the plasma radiation mainly depends on the temperature and density, which are constant on equilibrium flux surfaces in normal plasma conditions, it means that iso-emissivity contours are consistent with the flux surfaces and such a physical-based symmetry can be incorporated in a straightforward way in mathematical inversion methods. A typical method adopting such an assumption is Equilibrium-Based-Iterative-Tomography-Algorithm (EBITA) [2] which uses the equilibrium flux surfaces derived at the same measurement time as the starting point for the search of solution with more reasonableness in physics. Other successful methods such as Minimum Fisher Regularization (MFR) [3] and the Maximum Entropy (MaxEnt) [4] are based on numerical iterative algorithms with the intrinsic drawback of high computational time cost. By contrast, a Bayesian tomography method using a GP prior developed within Minerva Bayesian inference framework [5] has the potential for real-time application under an approximate optimization state, in particular with an enhanced capability for uncertainty analysis in the probability form [6].

2. Method

2.1 Tomography problem

In the HL-2A tokamak a Bayesian tomography method has been applied to the soft X-ray (SXR) system that constitutes two detector arrays and each one has 20 LOS, yielding full coverage of the plasma in the poloidal cross-section (see Fig. 1). The aim of the tomography problem is to compute the emissivity distribution expressed as $f(R, Z)$ from the line-integrated data,

$$d_l = c_l \int_{S_l} ds f(R, Z), \quad l = 1, 2, \ldots, M, \tag{1}$$

where M is the number of line-integrated data and the in-

author's e-mail: lid@swip.ac.cn

*) This article is based on the presentation at the 30th International Toki Conference on Plasma and Fusion Research (ITC30).

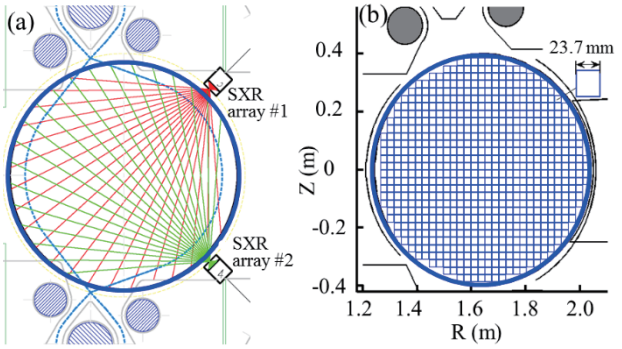

Fig. 1 (a) The coverage of 40 LOS from the SXR diagnostic on HL-2A and (b) finite-element discretization of the reconstructed region adopted in the method.

tegral is along the path of the viewing chord indexed by l. Mathematically, equation (1) is referred to as the Fredholm equation of the first kind, which concerns the solution of $f(R,Z)$ from its known integral values with fixed integration limits.

In Fig. 1 the region to be reconstructed is discretized into a grid of $N = 900$ square pixels. The size of the pixels is small enough to justify the assumption of constant emission within each pixel. The extension of the reconstructed region is chosen to cover the whole plasma cross-section within the Last Closed Flux Surface (LCFS). In our case, the choice of the dimension number $N = 900$ is a trade-off between computational efficiency and requirement of spatial resolution. For the boundary condition, the emission around the LCFS is set to be zero according to the fact that SXR emission is impossible in the temperature range of plasma edge. As a result, the equation (1) can be converted to a matrix form,

$$\overline{d}_M = \overline{\overline{R}}_{M\times N} \cdot \overline{f}_N, \tag{2}$$

where $\overline{\overline{R}}_{M\times N}$ is the mapping matrix derived from a forward model based on the geometry of LOS. The task of the calculation is to infer the most probable values of the free parameters $\overline{f}_N$ from a limited number of line-integrated data $\overline{d}_M$ under the condition of $N \gg M$.

2.2 Bayes' theorem and Gaussian Process

Bayesian probability theory provides an important guidance for the data analysis problems in different scientific fields as expounded in [7]. According to the Bayes' theorem, a posterior probability over the quantity of interest, i.e. the emission values f in equation (1), is equal to the product of a prior and a likelihood, divided by an evidence term,

$$p\left(f|d,\theta\right) = \frac{p\left(d|f,\theta\right)p\left(f|\theta\right)}{p\left(d|\theta\right)}, \tag{3}$$

where the prior $p(f|\theta)$ represents our knowledge about f before obtaining any data. This prior is modified by the measurements through the likelihood $p(d|f,\theta)$, representing our state of knowledge about f in the light of data d. Hyperparameter θ are parameters of the prior and need to be optimized through maximization of the evidence term $p(d|\theta)$.

As described above, a prior is required to be specified for the emission values f in the Bayesian formalism. The specification of the prior is important, because it governs the properties (e.g. smoothness and continuity etc.) of the functions considered for the inference of f. Based on the nature of the tomography problem under study, a Gaussian process (GP) [8] is chosen as a prior to impose an effective smoothness regularization on the reconstruction. Since GP is a generalization of the Gaussian probability distribution to the function space, a GP prior enables the discrete values of emission $\overline{f}$ (denoted as a vector) to be modeled as a Gaussian distribution centered at the mean $\overline{\mu}_{prior}$ with a covariance matrix $\overline{\overline{\Sigma}}_{prior}$,

$$p\left(\overline{f}|\bar{\theta}\right) \propto \exp\left(-\frac{1}{2}\left(\overline{f}-\overline{\mu}_{prior}\right)^T \overline{\overline{\Sigma}}_{prior}^{-1}\left(\overline{f}-\overline{\mu}_{prior}\right)\right). \tag{4}$$

In general, the covariance matrix $\overline{\overline{\Sigma}}_{prior}$ can be derived from a variety of stationary covariance functions. One of them is the squared-exponential (SE) covariance function, which defines the covariance of any two random variables at positions $\bar{r}$ and $\bar{r}'$,

$$K_{SE}(d) = \sigma^2 \exp\left(-\frac{d^2}{2l^2}\right), d = \left\|\bar{r}-\bar{r}'\right\|, \tag{5}$$

where σ determines the magnitude of the function to be modeled; d denotes the distance between any pair of positions $\bar{r}$ and $\bar{r}'$, which is scaled by a constant length-scale l. Therefore, the GP using a stationary covariance function can only produce constant smoothness everywhere. To address the problem of varying smoothness among different regions, a non-stationary covariance function has been developed as the following,

$$K^{NS}\left(\bar{r},\bar{r}'\right) = \sigma^2 \left|\overline{\overline{\Sigma}}(\bar{r})\right|^{1/4} \left|\overline{\overline{\Sigma}}\left(\bar{r}'\right)\right|^{1/4} \left|\frac{\overline{\overline{\Sigma}}\left(\bar{r}\right)+\overline{\overline{\Sigma}}\left(\bar{r}'\right)}{2}\right|^{-1/2}$$
$$\exp\left(-(\bar{r}-\bar{r}')^T\left(\left(\overline{\overline{\Sigma}}(\bar{r})+\overline{\overline{\Sigma}}(\bar{r}')\right)\Big/2\right)^{-1}(\bar{r}-\bar{r}')\right), \tag{6}$$

where the local kernel matrix $\overline{\overline{\Sigma}}(\bar{r})$ is a function of spatial position, rather than a constant as applied in the stationary covariance functions. Computation of the local kernels at many positions is solved by a hierarchical model as detailed in [6]. For the practical application of this non-stationary GP tomography method, locally adaptive smoothness can be achieved to distinguish the different smoothness between plasma center and edge. As a consequence, the reconstruction accuracy can be improved significantly.

Under the assumption that the noise associated with the measured experimental data are normally distributed, the likelihood can be modeled as a Gaussian distribution centered at the measured data $\overline{d}_{meas}$ with a covariance matrix $\overline{\overline{\Sigma}}_d$,

$$p\left(\overline{d}\,|\bar{f},\bar{\theta}\right) \propto \exp\left(-\frac{1}{2}\left(\overline{\overline{R}}\,\overline{f}-\overline{d}_{meas}\right)^T \overline{\overline{\Sigma}}_d^{-1}\left(\overline{\overline{R}}\,\overline{f}-\overline{d}_{meas}\right)\right). \tag{7}$$

The diagonal elements of $\overline{\overline{\Sigma}}_d$ defines the data variance based on an error analysis of the measured data.

The combination of a GP prior with a Gaussian likelihood gives rise to a posterior which is again a Gaussian distribution with a posterior mean,

$$\overline{m}_{post} = \overline{m}_{prior} + \left(\overline{\overline{R}}^T \overline{\overline{\Sigma}}_d^{-1} \overline{\overline{R}} + \overline{\overline{\Sigma}}_{prior}^{-1}\right) \times \overline{\overline{R}}^T \overline{\overline{\Sigma}}_d^{-1}\left(\overline{d}_{meas} - \overline{\overline{R}}\overline{m}_{prior}\right), \tag{8}$$

and a posterior covariance matrix,

$$\overline{\overline{\Sigma}}_{post} = \left(\overline{\overline{R}}^T \overline{\overline{\Sigma}}_d^{-1} \overline{\overline{R}} + \overline{\overline{\Sigma}}_{prior}^{-1}\right)^{-1}. \tag{9}$$

After optimization of the hyper-parameters embedded in the prior, $\overline{m}_{post}$ yields maximum a posteriori (MAP) estimate which is considered as the most likely solution of $\overline{f}$ in the sense that it is nearest to the prior point $\overline{\mu}_{prior}$, and meanwhile, a satisfactory fitting of the measured data can be achieved by the predicted data through the functional relationship $\overline{\overline{R}}\overline{m}_{post}$. In addition, uncertainty of the solution is represented by the posterior covariance in equation (9). In this way, the result is completely analytic without any iterative algorithms, enabling it to be a fast approach to resolving the inverse problems. In the case when the assumption of normal distribution is strongly violated, a non-Gaussian prior needs to be taken into account for the prior. The combination of a non-Gaussian prior with the Gaussian likelihood will lead to a posterior probability distribution whose best estimate is more difficult to find. In this situation, the properties of the posterior probability needs be analyzed by drawing many samples from it through the computationally expensive Markov chain Monte Carlo (MCMC) method.

2.3 Singular-Value Decomposition (SVD)

As a powerful mathematical technique, the SVD is routinely used to explore the spatio-temporal features of the perturbations in emission distribution induced by MHD activity [3, 9, 10]. If the data to be analyzed is acquired in the form of time series from P channels and the selected time window comprises Q time points with a time interval Δt, then the data set can be represented as a matrix,

$$\begin{aligned}\overline{\overline{X}} &= [\overline{x}(0), \overline{x}(\Delta t), \ldots, \overline{x}((Q-1)\Delta t)] \\ &= \begin{bmatrix} x_1(0) & \cdots & x_1((Q-1)\Delta t) \\ \vdots & \ddots & \vdots \\ x_P(0) & \cdots & x_P((Q-1)\Delta t) \end{bmatrix}.\end{aligned} \tag{10}$$

The data set $\overline{\overline{X}}$ can be either raw or processed data subjected to specific treatment. For instance, the raw data could be the line-integrated data while the processed data could be the spatially resolved emission distribution expressed by the emission quantities from a number of pixels. In practice, the SVD can be employed to the raw data for the discovery of the hidden phenomena such as sawtooth and snake-like perturbations, or to a time series of reconstructions for the MHD mode analysis [11]. It's worthy to note that only if the spatial/temporal measure preserves in the rows/columns of the data set $\overline{\overline{X}}$ and the condition $M > N$ are satisfied, can the SVD be applied for its spectrum analysis.

Accordingly, the SVD can be used to extract information about the spatio-temporal features of the perturbations. Here each column of $\overline{\overline{X}}$ constitutes the emissivity from all the different pixels (position indices form one dimension) at the same time point and the rows correspond to the time series (time indices form another dimension). The spatial and temporal eigenvectors are contained in the columns of $\overline{\overline{U}}, \overline{\overline{V}}$. The spatial eigenvectors or "topos" represent the spatial spectrum of $\overline{\overline{X}}$, and the temporal eigenvectors or "chronos" represents the temporal spectrum. The total weight of one data set can be given by,

$$W_X = \sum_{i=1}^{M}\sum_{j=1}^{N} X_{mn}^2. \tag{11}$$

It is also known that the following relationship exists according to the property of SVD,

$$W_X = \sum_{i=1}^{K} S_k^2, \quad K = \min(M, N). \tag{12}$$

The relative weight of each component S_k can be calculated by,

$$R_k = \frac{S_k^2}{W_X}, \tag{13}$$

which is a useful quantity to indicate the significance of the different components coupled in the reconstructed emission distribution. If there is a pair of identical singular values, namely the degeneration of solution exists, it suggests the existence of dynamic components such as rotating MHD modes. Therefore, the temporal evolution of the rotating modes can be revealed by taking into account their corresponding "chronos". The method developed in this work uses a GP prior to model the emission distribution such that the final solution is expressed in a probabilistic form, i.e. a posterior probability from which many samples of the reconstruction can be generated. The spread of

these samples can be taken as an effective way to visualize the uncertainty of the result.

3. Application

3.1 MHD mode analysis

In experiments of HL-2A, different kinds of MHD instabilities are often observed during neutral beam injection (NBI) heating [12–14]. Among them, the Long-lived mode (LLM) and fishbone mode are a typical internal kink instabilities induced by the resonance between the toroidal wave velocity of the modes and the toroidal precession frequency of trapped energetic particles from NBI injected beam. This instability mode would cause a radial displacement of the equilibrium flux surface and the rotation of this mode within laboratory frame transfers the spatial variation due to the mode to a temporal oscillation which can be recorded by the high frequency signals of SXR detector and Mirnov magnetic coils as shown in Fig. 2. Here the rotating mode at a flux surface with $q = m/n$ can be described in the following form [15, 16],

$$(m\theta - n\phi + 2\pi f_{(m,n)}t) = const, \tag{14}$$

where $f_{(m,n)}$ is the mode frequency in the laboratory frame. Due to the helical structure of the instability mode, both toroidal (ω_ϕ) and poloidal (ω_θ) rotation components contribute to $f_{(m,n)}$,

$$2\pi f_{(m,n)} = n\omega_\phi - m\omega_\theta, \tag{15}$$

where m, n and $f_{(m,n)}$ are the physical parameters to be analyzed. According to the torque input by NBI, the toroidal plasma rotation is estimated to be in the order of several kHz. By contrast, the poloidal plasma rotation is negligible as it is strongly damped in the plasma core. In Fig. 3 the mode structure are visualized through the perturbed emission distribution which are decoupled from the equilibrium component by means of the SVD analysis on 100 consecutive reconstructions within a time window of 1 ms. As shown, the mode rotates in the counter-clockwise direction at the $m/n = 1/1$ surface and completes one cycle in less than 0.1 ms in correspondence to the 12 kHz from the spectrogram of Mirnov signal as displayed in Fig. 2.

3.2 Analysis of impurity transport

The study of impurity transport has been conducted in HL-2A experiments with the aid of the Laser-Blow-Off (LBO) technique. In experiments with the injection of trace aluminum (Al) impurity by LBO, besides the bremsstrahlung emission emitted arising from electrons the line radiation from Al ions will also contribute strongly or even dominate the measured radiation in the SXR range. Therefore, the impurity density n_{Al} can be derived from the increment in emission after the injection based on a simplified emission model $\varepsilon_{Al}^{sxr} = n_{Al} n_e L_{Al}^{sxr}$ [17], where L_{Al}^{sxr} is the radiation coefficient with the dependence only on the electron temperature which is almost constant in time

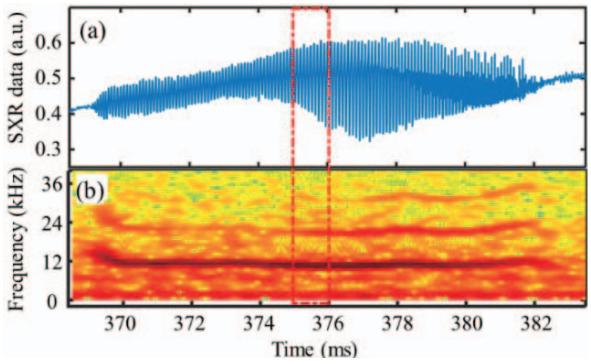

Fig. 2 Observation of an $m/n = 1/1$ internal kink mode in the phase of 0.8 MW NBI heating from shot #22493: (a) time trace of the SXR data from a channel passing through the plasma center and (b) frequency spectrum of the Mirnov coil signal.

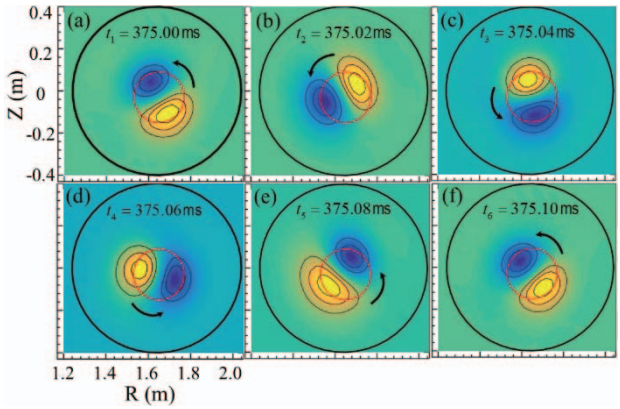

Fig. 3 Evolution of the $m/n = 1/1$ internal kink mode structure during a rotation cycle resolved by the SVD analysis of 100 consecutive SXR reconstructions in the time window of 1 ms (marked by the red rectangle in Fig. 2). The red circles indicate $q = 1$ surface.

during the time window of interest. It is thus reasonable to assume that there is an approximately linear relationship between n_{Al} and ε_{Al}^{sxr}, provided that the variation of n_e is also small. The time evolution of Al impurity density $n_{Al}(r, t)$ after the injection can be derived from the increase in emission. Therefore, the emission after subtracting the background contribution prior to the Al injection can be used to study the impurity transport. As shown in Fig. 4 both the increase in electron temperature induced by central Electron Cyclotron Resonance Heating (ECRH) and the injection of Al trace impurity at 600 ms can lead to an dramatic increase in the line-integrated SXR emission.

More precise information on the impurity density profile can be acquired from the 2D SXR emission reconstruction displayed in Fig. 5. In addition, the uncertainty of the reconstruction, which accounts for both the sparsity and the error of the line-integrated data, can be derived from the variance of a posterior probability (see equation (9)) as shown by the shaded area. At the maximum emission after

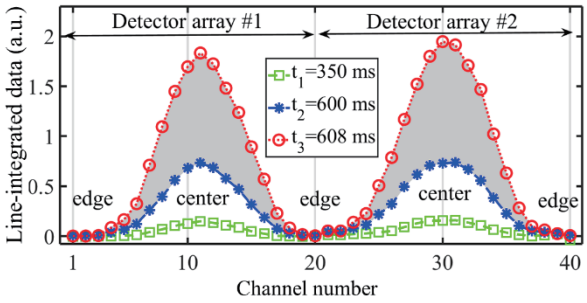

Fig. 4 Profiles of the line-integrated data from two SXR detector arrays at three representative time points: before central ECRH (t_1, green squares), during central ECRH (t_2, blue stars), and at the maximum of emission after trace *Al* injection (t_3, red circles).

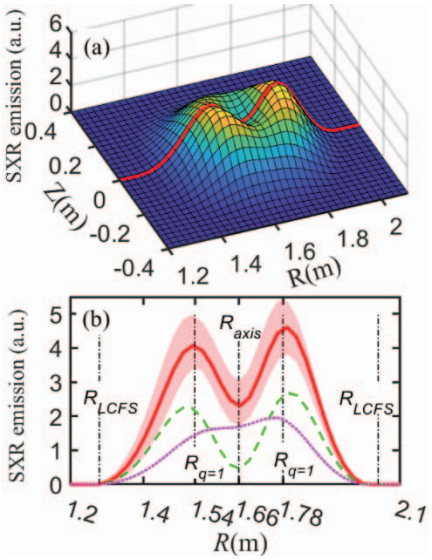

Fig. 5 SXR reconstruction after the injection of trace *Al* impurity during the phase of central ECRH and (b) the profiles of total emission (red solid line) with its uncertainty marked by the shaded area, background emission (green dashed line) and background-subtracted emission (magenta dotted line).

Al injection, the background-subtracted SXR reconstruction appears to be deeply hollow indicating that most of the *Al* impurity accumulates within the $q = 1$ surface (radial position $\rho \sim 0.3$), and only very few penetrates into the plasma center due to the strong expulsion of impurity by the core MHD instability [18]. For circular plasma cross-section of HL-2A, the radial transport equation in cylindrical coordinate can be used to calculate the *Al* impurity particle flux at different radial positions [19, 20],

$$\frac{\partial n_{Al}(r,t)}{\partial t} = -\frac{1}{r}\frac{\partial}{\partial r}(r\Gamma_{Al}(r,t)) + Q_{Al}(r,t), \qquad (16)$$

with the radial coordinate $r = \sqrt{V_{flux}/(2\pi^2 R_{axis})}$ where V_{flux} is the volume within the flux surface and R_{axis} is the major radius of the plasma axis. In the plasma core the source term $Q_{Al}(r,t) = 0$, thus equation (16) can be used to evaluate the total impurity flux,

$$\Gamma_{Al}(r,t) = -\frac{1}{r}\int_0^r \frac{\partial n_{Al}(r',t)}{\partial t} r' dr'. \qquad (17)$$

In our analysis the SXR reconstructions at 601 ms and 602 ms are used to calculate the time derivative in equation (17). The relative values of the *Al* impurity flux are calculated to be 3.6 and 8.6 at two different radial positions $\rho = 0.2$ and $\rho = 0.4$, respectively, suggesting that the latter has a strong inward impurity flux than the former.

4. Summary

In this work a Bayesian tomography method using a GP prior for smoothness regularization has been developed and applied to the SXR diagnostic on HL-2A. The improved accuracy of the reconstructions by this method allows one to obtain accurate information about the spatio-temporal features of the internal kind modes in terms of shape, location and rotation. In addition, impurity transport has been studied based on the emission model of impurity radiation and the radial transport equation. Experimental evidence shows that impurity density profiles appear to be deeply hollow in plasmas with central ECRH, which is postulated to arise from a combined effect of the expulsion of impurity by core MHD in the plasma center and an inward impurity convection driven by turbulence in the confinement region.

Acknowledgement

The authors acknowledge the support of the HL-2A team. This work is supported by National Science Foundation of China (Nos.12075078, 12075080 and 11875018), National magnetic confinement fusion Science Program of China (2019YFE03010003).

[1] K. Bockasten, J. Opt. Soc. Am. **51**, 943 (1961).
[2] A.P. Navarro *et al.*, IEEE Trans. Plasma Sci. **19**, 569 (1991).
[3] M. Anton *et al.*, Plasma Phys. Control. Fusion **38**, 1849 (1996).
[4] K. Ertl *et al.*, Nucl. Fusion **31**, 1477 (1996).
[5] J. Svensson and A. Werner, IEEE Workshop on Intelligent Signal Proc. (2007).
[6] D. Li *et al.*, Rev. Sci. Instrum. **84**, 083506 (2013).
[7] U. von Toussaint, Rev. Mod. Phys. **83**, 943 (2011).
[8] C.E. Rasmussen and C. Williams, *Gaussian Processes for Machine Learning* (MIT Press, 2006).
[9] C. Nardone *et al.*, Plasma Phys. Control. Fusion **34**, 1447 (1992).
[10] Y. B. Dong *et al.*, Plasma Sci. Technol. **6**, 2307 (2004).
[11] M. Bessenrodt-Weberpals *et al.*, Plasma Phys. Control. Fusion **38**, 1543 (1996).
[12] X.T. Ding *et al.*, Nucl. Fusion **42**, 491 (2002).
[13] W. Chen *et al.*, Nucl. Fusion **49**, 075022 (2009).
[14] L.M. Yu *et al.*, Nucl. Fusion **57**, 036023 (2017).
[15] V. Igochine, *Investigation of MHD Instabilities in Conventional and Advanced Tokamak Scenarios on ASDEX Up-*

grade (Technology University of Munichen, 2002).
[16] V. Igochine, *Active Control of Magneto-hydrodynamic Instabilities in Hot Plasmas* (Springer, Berlin, 2015).
[17] R. Dux *et al.*, Plasma Phys. Control. Fusion **45**, 1815 (2003).
[18] M. Sertoli *et al.*, Plasma Phys. Control. Fusion **57**, 075004 (2015).
[19] R. Dux, *STRAHL User Manual Laborbericht 10/30* (IPP, Garching, 2006).
[20] M. Sertoli *et al.*, Plasma Phys. Control. Fusion **53**, 035024 (2011).